Materials Horizons

ROYAL SOCIETY OF CHEMISTRY

COMMUNICATION

View Article Online
View Journal

Check for updates

Cite this: DOI: 10.1039/d5mh02371h

Received 10th December 2025,
Accepted 27th May 2026

DOI: 10.1039/d5mh02371h

rsc.li/materials-horizons

Open Access Article. Published on 03 June 2026. Downloaded on 6/4/2026 12:36:40 AM.
This article is licensed under a Creative Commons Attribution 3.0 Unported Licence.

High-performance solution-processed TIIG-based polymer photodetector with detectivity across scalable SWIR applications

Rico Holfeuer, [ab] Marc Comi,[c] Stefan Schröder, [de] Meriem Bouraoui,[b] Johannes Hofmann, [b] Rik Hooijer, [b] Erkan Aydin, [b] Achim Hartschuh, [b] Mohammed Al-Hashimi,*[f] AmirAbbas YousefiAmin*[ab] and Tayebeh Ameri *[bde]

Developing cost-efficient, flexible, and Restriction of Hazardous Substances (RoHS)-compliant short-wave infrared (SWIR) photodetectors compatible with roll-to-roll processing remains a significant challenge. Here we present a simplified organic 'metal–semiconductor–metal' (MSM) photodetector featuring a single solution-processed bulk heterojunction of a newly synthesized thienoisoindigo-based ultralow-bandgap polymer, TIIG-Se-DFT, blended with the nonfullerene acceptor (NFA) Y6. The TIIG-Se-DFT polymer, incorporating selenophene and fluorinated thiophene units, combines a narrow bandgap of 0.96 eV with strong absorption across 700–1600 nm and forms films with local molecular order, enabling broadband light harvesting without multistep layer stacking. Device simplicity is achieved using an interdigitated Au electrode and a single solution-processed active layer, minimizing vacuum deposition and eliminating interlayer damage due to solvent exposure. The resulting photodetector reaches a specific detectivity (D^*) of $\approx 2 \times 10^{11}$ Jones at 1150 nm, retains $> 0.13 \times 10^{10}$ Jones at the eye-safe 1550 nm telecom band, and delivers 86/36 μs rise/fall times at 1 V_{bias}. Dark current is held to 4.6×10^{-8} A cm^{-2}, and encapsulated devices preserve >95% responsivity after 800 hours of ambient aging. The simplified, high-sensitivity processing advances TIIG-Se-DFT:Y6 SWIR photodetectors toward industrial scale suitable for wearables, light detection and ranging (LiDAR), and optical communications.

New concepts

This work presents a new concept for simplified and scalable organic SWIR photodetectors by combining targeted polymer design with a minimal device architecture. We developed a broadband photodetector using a newly synthesized thienoisoindigo-based polymer (**TIIG-Se-DFT**) with selenophene and fluorinated thiophene units, blended with Y6 into a single bulk heterojunction. In contrast to typical vertical multilayer stacks, our concept uses a horizontal MSM layout with interdigitated Au electrodes and a single solution-processed absorber layer. This reduces fabrication complexity, eliminates solvent-induced interlayer damage, and enables compatibility with roll-to-roll processing. With broadband absorption from 700 to 1600 nm and a specific detectivity of $\approx 0.2 \times 10^{12}$ Jones at 1150 nm, the device reaches performance levels of industrial relevance. This concept shows that combining ultralow-bandgap polymer design with a simplified device layout is sufficient to access high SWIR sensitivity and device stability. The concept provides a platform toward RoHS-compliant, scalable NIR-to-SWIR detection for future wearable sensing, LiDAR, and optical communication applications.

1. Introduction

The near-infrared (NIR) and short-wave infrared (SWIR) spectral windows (≈700–1600 nm) are crucial for numerous emerging technologies, such as optical communication, LiDAR, wearable biomedical imaging, and environmental sensing. In particular, the SWIR range enables deep tissue penetration, negligible autofluorescence, and enhanced spatial resolution compared to standard NIR approaches.[1] The 1550 nm wavelength stands out as it falls within an atmospheric transmission window, is classified as eye-safe, and is widely used in long-range communications and imaging systems.[2] While conventional inorganic photodetectors, typically based on InGaAs, PbSe, and cadmium compounds, offer excellent spectral response, their integration in flexible and cost-sensitive applications is limited by high

[a] Serino Tech (LMU deep-tech startup), Munich, Germany. E-mail: amir.amin@cup.uni-muenchen.de
[b] Department of Chemistry and Center for NanoScience (CeNS), University of Munich (Ludwig-Maximilians-University (LMU)), Butenandtstraße 5–13, 81377, Munich, Germany. E-mail: tam@tf.uni-kiel.de
[c] Flemish Institute for Technological Research (VITO N.V.), Boeretang 200, Mol 2400, Belgium
[d] Chair of Composite Materials, Department of Materials Science, Faculty of Engineering, Christian-Albrechts-Universität zu Kiel, Kaiserstrasse 2, 24143, Kiel, Germany
[e] Kiel Nano, Surface and Interface Science KiNSIS, Kiel University, Christian-Albrechts-Platz 4, D-24118, Kiel, Germany
[f] College of Science and Engineering, Hamad Bin Khalifa University, Doha, Qatar. E-mail: malhashimi@hbku.edu.qa

Open Access Article. Published on 03 June 2026. Downloaded on 6/4/2026 12:36:40 AM. This article is licensed under a Creative Commons Attribution 3.0 Unported Licence.

production costs, rigidity, toxicity concerns, and constrained scalability.[3,4] These drawbacks underscore the urgent need for environmentally friendly and affordable materials that meet the requirements of next-generation technologies such as portable photoplethysmography (PPG) and point-of-care diagnostics.[5] However, the precise molecular design principles that enable organic semiconductors to maintain high SWIR detectivity while preserving processability remain underexplored. In this context, organic photodetectors (OPDs) have emerged as promising candidates due to their mechanical flexibility, biocompatibility and processability *via* scalable fabrication technologies. These attributes position OPDs for use in large, cost-sensitive markets, including consumer electronics, wearable systems, and portable diagnostic platforms.[6] OPDs, particularly those employing bulk heterojunction (BHJ) architectures, have attracted considerable attention for their tunable optical properties, scalable solution processability, and inherent compatibility with flexible substrates.[7,8] Nevertheless, achieving broad spectral sensitivity extending into the NIR-to-SWIR region, while maintaining high detectivity and ease of fabrication remains a persistent challenge for existing OPDs. Current state-of-the-art organic thin film SWIR photodiodes employ complex vertical multilayer stacks, which require multiple vacuum-deposited layers or sequential solution processing steps.[9–11] These multilayer configurations introduce significant fabrication complexity and raise concerns regarding long-term device stability. In particular, sequential deposition of solution-processed layers poses inherent risks:[12–14] Solvent interactions during upper layer coating can disrupt previously deposited layers, leading to crystallization anomalies, interfacial roughness, defect formation, and even partial dissolution or swelling of the underlying film. Together, these effects compromise device integrity, electrical performance, and scalability, limiting the broader adoption of such architectures in cost-sensitive or flexible applications. To overcome these challenges, we present a simplified lateral MSM device architecture utilizing an interdigitated electrode (IDE) combined with a single, solution-processed BHJ active layer. Compared with vertically stacked multi-layer configurations, this lateral approach simplifies fabrication and lowers manufacturing cost while maintaining device performance compatible with integration into optoelectronic integrated circuits.[15,16] A key trade-off *versus* vertical PIN photodiodes is that MSM detectors have no significant built-in junction field and therefore typically require an externally applied lateral field across the IDE gap (*i.e.*, volt-level biasing) for efficient extraction, whereas PIN diodes can operate at 0 V (photovoltaic mode) or modest reverse bias.[17,18] The higher bias can increase power consumption and can raise dark current *via* bias-enhanced injection and Schottky-barrier lowering.[17,19] Furthermore, photoconductor-type MSM operation may exhibit gain mechanisms arising from long-lived trapped carriers, potentially resulting in a reduced temporal response compared to vertical junction photodiodes.[16,20] Nevertheless, restricting solution processing to a single active layer avoids multi-step wet processing and associated interlayer compatibility constraints, helping preserve film morphology and improving reproducibility. This, combined with only one vacuum-deposited electrode and ambient-compatible coating, makes the approach well aligned with scalable manufacturing routes.[15,16] Therefore, the lateral MSM configuration not only improves reproducibility and device robustness but also marks a departure from conventional vertical OPD stacks, positioning it as a promising platform for next-generation SWIR sensing technologies.

Since its introduction, thienoisoindigo (TIIG) has emerged as one of the most promising electron-deficient building blocks in organic semiconductor research. Originally derived from isoindigo, TIIG addresses key limitations of the parent structure, such as its twisted backbone and limited light absorption, which arise from steric hindrance between the phenyl and carbonyl groups.[21] By substituting the terminal phenyl rings with thiophene units, TIIG achieves improved molecular planarity and stronger π-conjugation, resulting in narrower optical bandgaps and broader absorption spectra.[22] These improvements promote greater charge delocalization and intermolecular interactions, making TIIG-based materials excellent candidates for organic field-effect transistors (OFETs),[23] organic photovoltaics (OPVs),[24] and increasingly, in organic photodetectors. Compared to isoindigo and other electron-deficient cores (*e.g.*, diketopyrrolopyrrole, naphthalene diimide), TIIG offers several advantages: (i) strong NIR optical absorption ($\lambda_{cut\text{-}off} > 1100$ nm), (ii) favorable edge-on stacking in thin films, (iii) high ambipolar charge mobility, and (iv) broad chemical tunability *via* donor/acceptor (D)–(A) backbone modifications.[22,25] Incorporation of selenophene units,[26–29] fluorinated aryl rings such as fluorobenzenes and fluorothiophenes[30,31] or fused aromatic units[22,32] (*e.g.* benzothienoisoindigo) further extended the absorption of thiophene- and TIIG-based materials into the SWIR region. These structural modifications simultaneously improve the rigidity of the backbone structure and the polymer stacking order as well as narrow the optical bandgap. However, despite the remarkable photophysical properties of TIIG-based conjugated materials and their demonstrated NIR-SWIR absorption in solution and thin films, reports of TIIG-based photodetectors, especially in the SWIR regime, remain rare. To date, only four reports describe TIIG-based infrared photodetectors. Among them, only the work of Han *et al.*[33] demonstrates SWIR detection extending to ≈1600 nm. Their device employs a carefully designed vertical multilayer architecture with multiple vacuum-deposited interlayers and electrodes, though such complexity could make large-scale implementation more demanding. The other three studies focus on NIR operation with limited detection range ($\lambda_{cut\text{-}off} \approx$ 900 nm)[34–36] falling short of the SWIR region. Han *et al.* achieved this response by combining the TIIG acceptor with larger fused donor motifs and thiophene bridging units to extend π-conjugation, improve backbone linearization, and reduce the bandgap in a complex vertical multilayer photodiode architecture. In contrast, the present work combines selenium-enhanced orbital delocalization and fluorine-induced conformational locking in **TIIG-Se-DFT** to promote backbone planarity, strengthen intramolecular charge transfer, and enable intrinsic deep-SWIR absorption, together with a simplified single-layer MSM architecture that avoids additional interfacial layers and vacuum-steps. This approach reduces fabrication

 This journal is © The Royal Society of Chemistry 2026

Open Access Article. Published on 03 June 2026. Downloaded on 6/4/2026 12:36:40 AM. This article is licensed under a Creative Commons Attribution 3.0 Unported Licence.

complexity and mitigates solvent-induced interlayer damage, while maintaining efficient charge generation and extraction within the bulk heterojunction. Although commercial InGaAs SWIR photodetectors remain the benchmark for absolute performance, recent laboratory-scale organic SWIR photodiodes have reported specific detectivities up to 1.71×10^{13} Jones at 1110 nm and 1.1×10^{13} Jones at 1100 nm in optimized vertical architectures.[37,38] While MSM devices do not yet reach these champion values, the present **TIIG-Se-DFT**:Y6 photodetector still delivers technologically relevant SWIR performance in a structurally simple single-layer architecture, highlighting its promise for scalable manufacturing.

These observations served as motivation to develop TIIG-based SWIR OPDs that convert intrinsic SWIR absorption into broadband device response while supporting scalable, printing-compatible processing and simplified architectures. In this study, we introduce **TIIG-Se-DFT**, a new member of the TIIG family. Incorporating selenophene and fluorinated thiophene units yields a planar backbone, improved charge mobility, and broadband absorption extending into the SWIR ($\approx$1600 nm). The benchmark NFA Y6 was selected not as the primary deep-SWIR absorber, but as a benchmark nonfullerene acceptor that provides complementary absorption, favorable energy-level alignment with **TIIG-Se-DFT**, and reliable electron-transport pathways within the bulk heterojunction. The resulting photodetector demonstrates competitive SWIR performance. This is highlighted by a specific detectivity of $\approx 0.2 \times 10^{12}$ Jones at 1150 nm, and $> 0.13 \times 10^{10}$ Jones at 1550 nm. The encapsulated devices also exhibit rapid sub-100 μs response times, and exceptional operational stability exceeding 800 hours under ambient conditions. Through comprehensive structural, optical, and morphological characterizations, we validate the performance and robustness of this scalable photodetection platform. Our findings underscore the substantial potential of TIIG-based polymers, particularly **TIIG-Se-DFT**, as sustainable, high-performance solutions for biomedical diagnostics, optical communications, and emerging wearable sensing applications. Here, we show that the deliberate introduction of selenophene and fluorinated thiophene units into a TIIG-based backbone establishes a clear structure–property-performance correlation, enabling deep SWIR absorption, suppressed dark current, and long-term device stability.

2. Results and discussion

2.1. Design, synthesis, and comprehensive characterization of the ultralow bandgap polymer TIIG-Se-DFT for NIR-to-SWIR photodetection

The development of a simplified, scalable NIR-SWIR photodetector architecture requires low-bandgap polymers that combine ambient-processable fabrication, RoHS compliance, and broad spectral sensitivity, requirements that remain unmet by conventional inorganic semiconductors. To address this gap, we designed a new conjugated polymer that exhibits extended NIR-SWIR absorption and compatibility with cost-effective manufacturing. Our molecular design integrates three chemically synergistic building blocks (Fig. 1): a thienoisoindigo-based (A) unit (TIIG),[39] a fluorinated thiophene functionalization unit (DFT) and a selenophene-based (D) unit (DTD-Se). The TIIG unit was selected for its pronounced electron-deficient character and high electronegativity contributing to a robust, planarized backbone.[39] The DTD-Se unit features an electron-rich selenophene moiety, enhancing molecular orbital overlap and facilitating efficient intramolecular charge transfer.[26–29] Strategic incorporation of the DFT unit optimized the polymer's electronic and morphological properties. Owing to fluorine's high electronegativity and compact van der Waals radius, intramolecular F···S/H contacts are favored, increasing backbone planarity and promoting charge delocalization. These combined effects intensify intermolecular noncovalent interactions, yielding a reduced optical bandgap and stronger absorption in the NIR-SWIR range.[30,31] The TIIG : DTD-Se : DFT molar ratio of 1 : 0.80 : 0.20 was selected to balance backbone planarity and conformational flexibility. The DTD-Se unit modulates electronic delocalization and torsional freedom, whereas DFT contributes greater conformational locking and segment directionality. Preliminary evaluation of alternative DTD-Se/DFT ratios (*e.g.*, 0.5/0.5 and 0.7/0.3) indicated that higher DTD-Se content increased torsional disorder and broadened absorption, while higher DFT fractions led to slightly blue-shifted absorption consistent with increased rigidity. The 0.80/0.20 composition provided the best compromise between aggregation, energetic alignment, and device performance. The resulting polymer, **TIIG-Se-DFT**, was synthesized *via* a Stille coupling reaction (Fig. 1).

Calculations based on the extended tight-binding semi-empirical xtb method[40] and ωB97X-D4/def2-SVP level[41] density functional theory were used to examine oligomers and the stacking of **TIIG-Se-DFT** derived fragments. To keep the models tractable and reduce computational complexity, branched alkyl groups were replaced with methyl substituents, as also reported in the literature for similar molecules.[9] Fig. 2a and b show the optimized geometries of a selected dimer and trimer, highlighting backbone planarity and torsional angles for the relevant repeat units (TIIG-DFT, TIIG-DTD-Se, and their combinations). The dimers illustrate the typical dihedral arrangements between repeating units, while the trimers capture conformational features emerging at the 3-unit level, including partial self-stacking tendencies. The latter are shown in the SI (Fig. S1) to provide an additional view of the oligomer conformations. To further substantiate the proposed role of intramolecular noncovalent interactions in enforcing backbone planarity, electrostatic potential (ESP) maps were computed for the presented dimer and trimer and mapped onto the electron density isosurface. Distinct regions of electrostatic complementarity are observed between adjacent units, supporting the presence of stabilizing S···O and/or Se···F interactions. In addition, localized positive potential at C–H sites in proximity to electron-rich atoms suggests the possible contribution of weak interactions.

In addition, key dihedral angles between repeating units (TIIG-DFT, DFT-DTD-Se, TIIG-DTD-Se) were extracted from these optimized oligomers and are provided in Table S1 (in SI),

Open Access Article. Published on 03 June 2026. Downloaded on 6/4/2026 12:36:40 AM.
This article is licensed under a Creative Commons Attribution 3.0 Unported Licence.

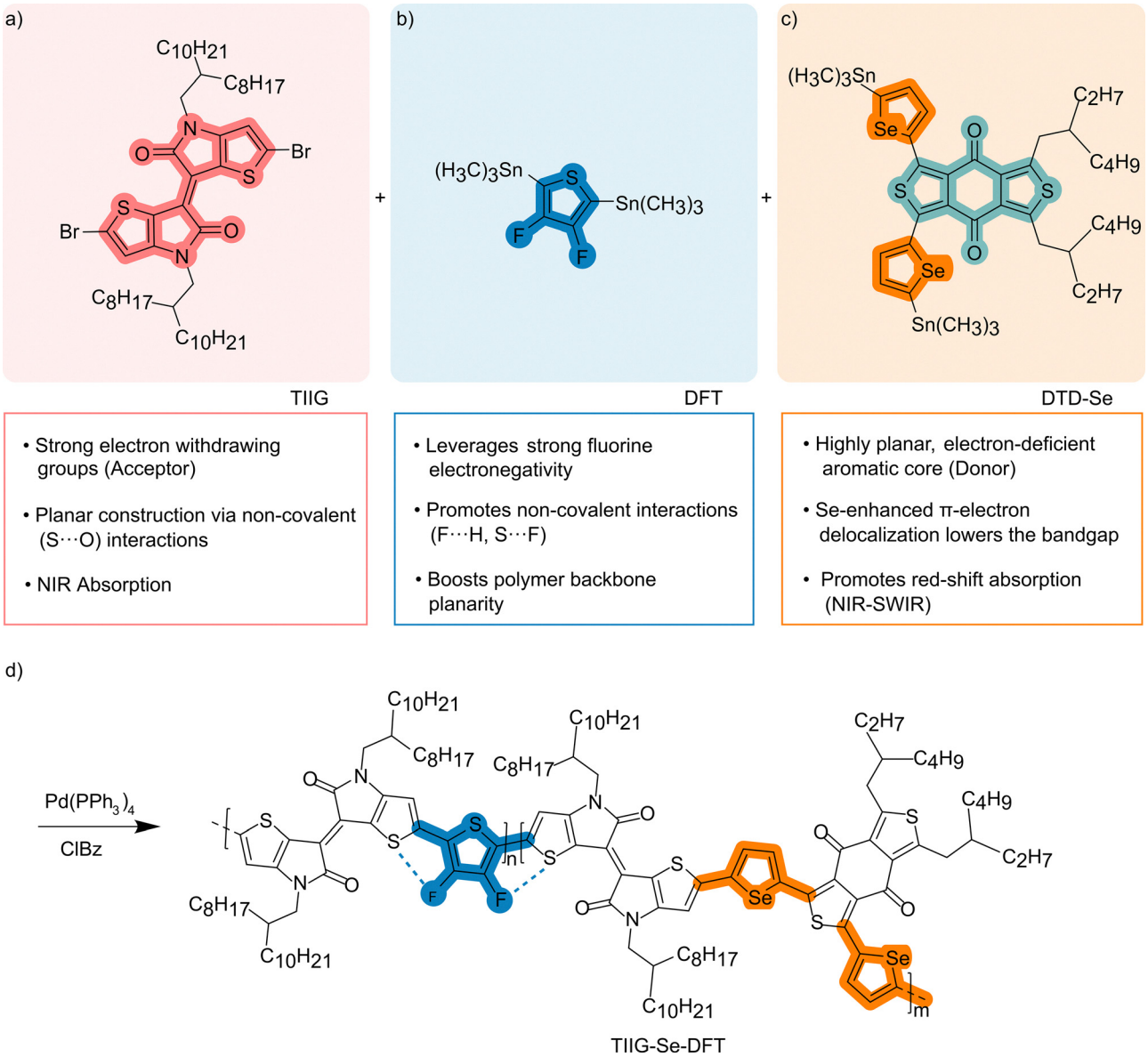

Fig. 1 Molecular building blocks and Stille coupling synthetic route of the novel **TIIG-Se-DFT** polymer. (a) A thienoisoindigo-based acceptor unit (TIIG, pink) to enforce backbone planarity, and drive NIR absorption. (b) A 3,4-difluorothiophene unit (DFT, blue) whose F···X (X = H, S) interactions lock the π-conjugated (D)–(A) backbone in a planar geometry. (c) A benzo[1,2-*c*:4,5-*c*′]dithiophene-4,8-dione donor unit (DTD-Se – teal/orange) flanked by selenophenes to enhance π-overlap, lower the bandgap, and red-shift into the NIR-SWIR. Monomers: 3,4-difluoro-2,5-bis(trimethylstannyl)thiophene (DFT) and 1,3-bis(5-trimethylstannylselenophen-2-yl)-5,7-bis(2-ethylhexyl)benzo[1,2-*c*:4,5-*c*′]dithiophene-4,8-dione (DTD-Se) are polymerized with the 2,2′-dibromo-4,4′-bis(2-octyldodecyl)-[6,6′-bithieno[3,2-*b*]pyrrolylidene]-5,5′(4*H*,4′*H*)-dione acceptor (TIIG) under Pd-catalysed Stille conditions. (d) Product: **TIIG-Se-DFT** low-bandgap (D)–(A) polymer.

revealing the range of backbone torsion present in the various arrangements. To further evaluate torsional flexibility along the polymer backbone, representative *syn* and *anti* conformers were analyzed for the key inter-unit linkages (TIIG–DFT, DFT–DTD-Se, and TIIG–DTD-Se). The corresponding dihedral angles and relative energies were extracted from the optimized dimer structures and are summarized in Table S2 (in SI). For all three linkages, the calculated energy differences between *syn* and *anti* conformations are small (<1 kcal mol^{-1}), indicating relatively shallow torsional potentials and suggesting that the backbone can readily adopt near-planar conformations. Such conformational flexibility is expected to facilitate effective π-conjugation and intermolecular electronic coupling in the polymer backbone.

The influence of backbone planarity on the electronic properties of the polymer was further analyzed by computing the frontier molecular orbitals (HOMO and LUMO) of a trimer, a dimer, the repeat units and the individual donor/acceptor segments (TIIG, DFT, DTD-Se). Torsional distortions between adjacent units reduce π-orbital overlap, effectively shortening the conjugation length, increasing the bandgap, and diminishing intrachain electronic coupling. In contrast, near-planar

 This journal is © The Royal Society of Chemistry 2026

Open Access Article. Published on 03 June 2026. Downloaded on 6/4/2026 12:36:40 AM.
This article is licensed under a Creative Commons Attribution 3.0 Unported Licence.

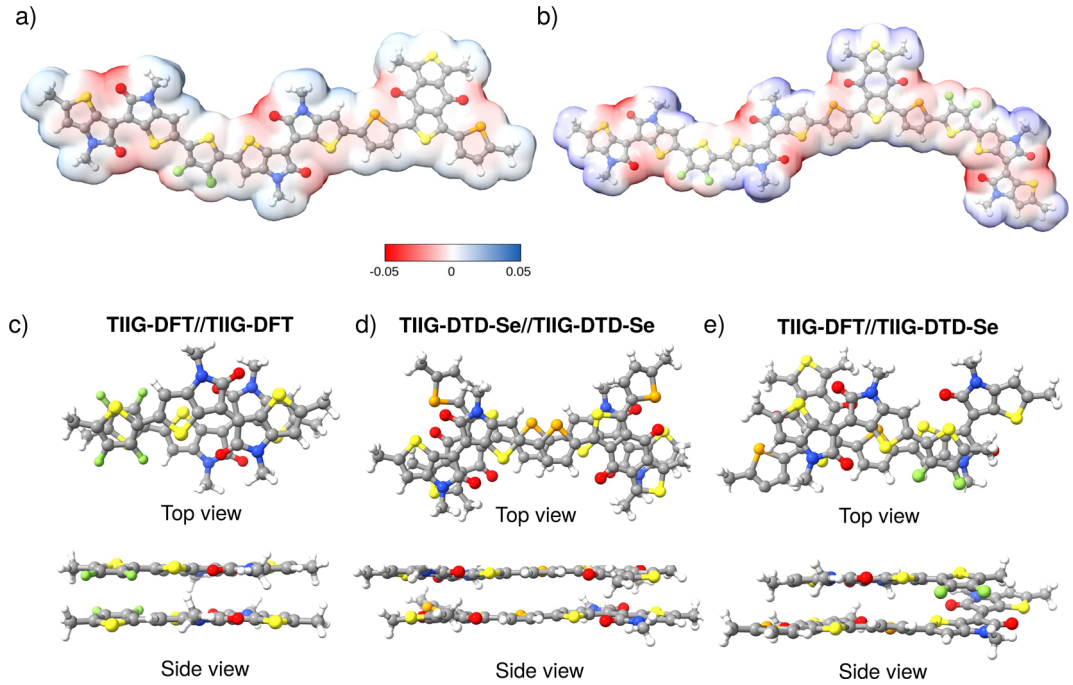

Fig. 2 Computationally optimized geometries and electrostatic surface potential (ESP) maps of (a) a selected dimer and (b) a selected trimer. Computationally optimized stacks of individual repeating unit: (c) TIIG-DFT//TIIG-DFT (repeating units A//A) and (d) TIIG-DTD-Se//TIIG-DTD-Se are cofacial and nearly coplanar (≈0°), whereas (e) the mixed TIIG-DFT//TIIG-DTD-Se is more twisted. Like–like (c and d) stacks are energetically favoured, consistent with stronger π–π coupling and better charge transport.

conformations maximize π-conjugation and promote delocalization of the frontier orbitals along the backbone, consistent with efficient intrachain charge transport. HOMO and LUMO energies of the individual segments, as well as of dimers and trimers, were extracted to illustrate the evolution of electronic levels with increasing oligomer length. Comparison of the segmental and repeat unit orbitals reveals the expected donor–acceptor character and highlights the alignment of energy levels that facilitates intrachain charge-transfer interactions (Table S3 in SI).

Fig. 2c–e depicts top and side views of dimer stacks assembled from the (A) repeating unit (TIIG-DFT) and the (D) repeating unit (TIIG-DTD-Se), respectively: TIIG-DFT//TIIG-DFT, TIIG-DTD-Se//TIIG-DTD-Se, and the mixed TIIG-DFT//TIIG-DTD-Se pair. The like-like assemblies (Fig. 2c and d) converge to nearly cofacial, coplanar arrangements with dihedral angles approaching 0°, consistent with local π–π stacking, especially favored by the sulfur–fluorine interactions in the TIIG-DFT units. The hetero-stack (Fig. 2e) is more twisted, exhibiting reduced planarity. However, this might also be associated with the different unit sizes leading to a folding up of the larger unit at the edges. Consistent with these geometries, the like-like stacks are the most stabilized (lowest interaction energies), whereas the hetero-stack is probably less favored. Such enforced coplanarity is expected to promote wavefunction delocalization and strengthen intermolecular π–π coupling, which can promote charge transport along stacked pathways and support locally higher order domains, especially when used in a donor-rich heterojunction blend. Accordingly, increased local ordering may narrow energetic disorder and reduce trap-mediated losses, consistent with the improved detectivity in the final devices.

Gel permeation chromatography (GPC) analysis determined the polymer's molecular weight (M_n) as 38 kDa with a dispersity ($Đ$) of 2.3, which is appropriate for device grade polymer thin films, ensuring optimized morphological and electronic characteristics. UV-vis-NIR spectra of **TIIG-Se-DFT** in solution and thin film (Fig. 3a) show a pronounced absorption band centered at 930 nm. From the solution to the film, an extended absorption profile with a $\lambda_{cut\text{-}off}$ of up to 1600 nm was observed. Efficient light harvesting is further evidenced by the high film absorption coefficient $\alpha \approx 1.1 \times 10^5$ cm^{-1} (for details see Section 2: comprehensive BHJ blend characterization for advanced NIR-to-SWIR photodetection and Fig. S2).

Cyclic voltammetry (Fig. 3b) revealed HOMO and LUMO energy levels of −4.71 eV and −3.72 eV, corresponding to an electrochemical bandgap E_g^{el} of 0.99 eV for the **TIIG-Se-DFT** polymer. Tauc analysis (Fig. 3c) yielded an optical bandgap E_g^{op} of 0.96 eV, consistent with the electrochemical bandgap. This value does not directly correspond to the long-wavelength absorption cut-off ($\lambda_{cut\text{-}off}^{film}$ = 1600 nm), which extends further into the SWIR due to sub-bandgap absorption. Together, these results highlight the material's potential for extended NIR-SWIR photodetection, particularly within technologically important ranges extending beyond conventional silicon detectors. The thermal properties, which significantly influence long-term device stability and fabrication conditions, were analyzed using thermogravimetric analysis (TGA) and differential scanning calorimetry (DSC). The TGA measurement demonstrates good

Open Access Article. Published on 03 June 2026. Downloaded on 6/4/2026 12:36:40 AM.
This article is licensed under a Creative Commons Attribution 3.0 Unported Licence.

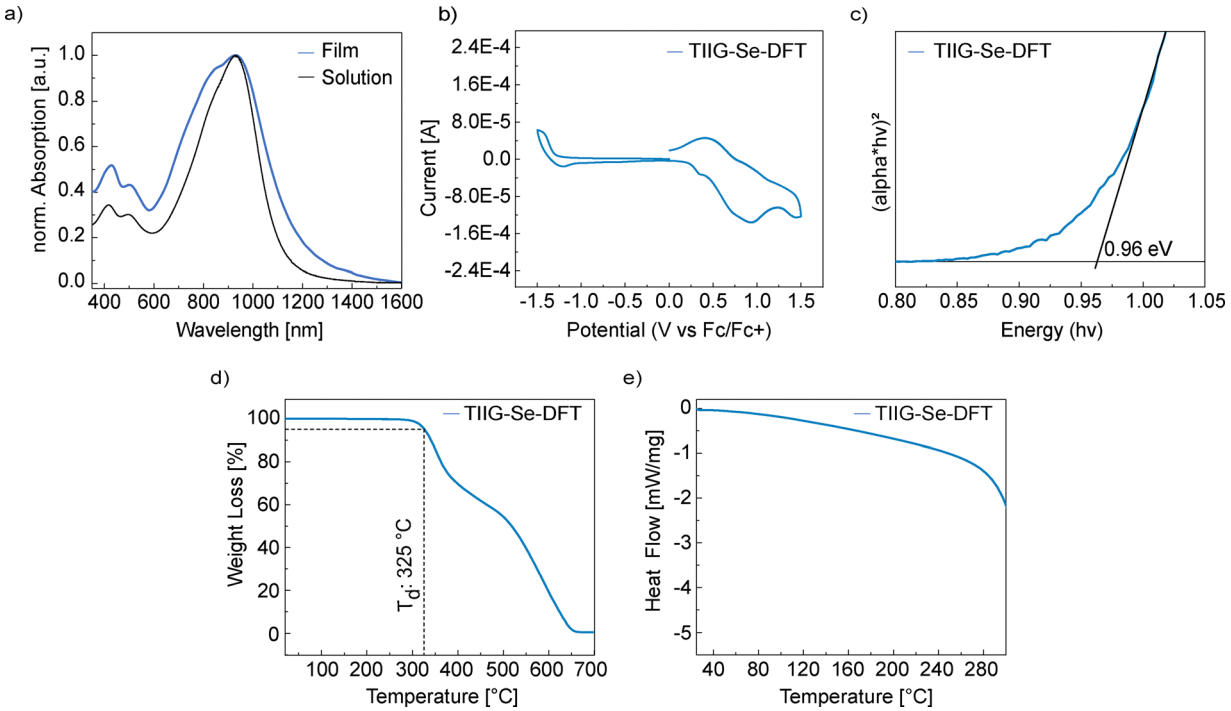

Fig. 3 (a) UV-vis-NIR absorption spectra of the polymer in solution and thin-film state. (b) Cyclic voltammogram (CV) of the **TIIG-Se-DFT** film. (c) Tauc plot diagram confirming an optical bandgap E_g^{op} of approximately 0.96 eV. (d) TGA measurement demonstrating good thermal stability of the **TIIG-Se-DFT** polymer with a decomposition temperature at 325 °C with 5% weight loss. (e) The corresponding DSC graph showcasing no apparent thermal transition observed in the range of 25 to 300 °C. Detailed molecular and photophysical parameters are summarized in Table 1.

thermal stability with a very high decomposition temperature, whereas just 5% weight loss is observed at 325 °C (Fig. 3d). The DSC thermogram shows no apparent thermal transition in the range of 25 to 300 °C (Fig. 3e), suggesting a highly stable, predominantly amorphous morphology with no evidence of long-range crystallinity over this range. Consequently, the key attributes of **TIIG-Se-DFT** include a facile synthesis *via* Stille coupling, an ultralow bandgap, a high absorption coefficient, high thermal stability, and good solution processability. A summary of key optical and thermal properties is provided in Table 1. Y6, used as the acceptor component in the final BHJ devices, is a well-established nonfullerene acceptor with widely reported thermal and structural properties. Literature DSC measurements show a defined melting transition at 295.5 °C and moderate crystallinity.[42]

Fourier-transform infrared (FTIR) spectroscopy further confirmed the chemical integrity and functionality of the **TIIG-Se-DFT** polymer, revealing distinct vibrational modes corresponding to its molecular backbone (Fig. S3). The strong absorption band at 1678 cm^{-1} corresponds to the C=O stretching vibration of the lactam (ketone) group in the thienoisoindigo (TIIG) unit, consistent with reported values around 1671 cm^{-1}.[43] The peaks at 1363 cm^{-1} and 1308 cm^{-1} are assigned to aromatic C–N stretching within the TIIG backbone, comparable to the C–N–C stretching observed at 1294 cm^{-1} in similar systems.[43] Vibrational bands at 1148 cm^{-1} and 1109 cm^{-1} can be attributed to C–F stretching from the fluorinated thiophene units, while additional peaks at 821, 783, and 756 cm^{-1} arise from C–H out-of-plane bending modes in the TIIG and thiophene rings. The aliphatic C–H stretching vibrations at 2958, 2924, and 2853 cm^{-1} confirm the presence of side-chain functionalities.[44]

Comprehensive chemical, structural, thermal, and optoelectronic analyses confirm that **TIIG-Se-DFT** is a well-defined, conjugated ultralow bandgap polymer engineered for high performance NIR-SWIR photodetection. Its tailored molecular design delivers strong NIR-SWIR absorption, favorable energy

Table 1 Key molecular and photophysical parameters of the **TIIG-Se-DFT** polymer

D–A polymer	M_n[a]	$Đ$[a]	$\lambda_{cut\text{-}off}^{sol}$ [nm][b]	$\lambda_{cut\text{-}off}^{film}$ [nm][c]	α-Abs-Coeff. [cm^{-1}]	HOMO[d] [eV]	LUMO[d] [eV]	E_g^{el} [eV][e]	E_g^{op} [eV][f]	T_d [°C][g]
TIIG-Se-DFT	38	2.3	1415	1600	1.1×10^5	−4.71	−3.72	0.99	0.96	325

[a] Molecular weight (M_n) and polydispersity ($Đ$) were determined by GPC. [b] $\lambda_{cut\text{-}off}^{sol}$ determined from dichlorobenzene solution. [c] $\lambda_{cut\text{-}off}^{film}$ of the film coated onto a glass substrate. [d] HOMO and LUMO energy levels obtained by referencing the onset oxidation and reduction potentials to the ferrocene/ferrocenium (Fc/Fc^+) redox couple, using $E_{HOMO} = -(E_{ox,onset} + 4.8)$ eV and $E_{LUMO} = -(E_{red,onset} + 4.8)$ eV. [e] Electrochemical bandgap: $E_g^{el} = E_{ox/onset} - E_{red/onset}$. [f] Optical bandgap: E_g^{op} was determined from Tauc plot analysis of the thin-film. [g] Decomposition temperature (T_d) obtained from TGA analysis.

This journal is © The Royal Society of Chemistry 2026

Open Access Article. Published on 03 June 2026. Downloaded on 6/4/2026 12:36:40 AM.
This article is licensed under a Creative Commons Attribution 3.0 Unported Licence.

level alignment, and good thermal stability, making it well suited for integration into advanced solution-processed organic photodetectors for applications in optical communications, biomedical diagnostics, flexible electronics, and wearable health monitoring.

2.2. Comprehensive BHJ blend characterization for advanced NIR-to-SWIR photodetection

Current state-of-the-art organic thin film SWIR photodiodes employ a PIN stack, anode/interfacial layer/active layer/interfacial layer/cathode, so even the most minimalist design contains ≥ 5 vertically stacked films (Table S4). Three of these layers, the transparent and reflective electrodes (ITO plus Au, Ag, or Al) and charge selective interlayers such as MoO_3, BCP, or C_{60}, must still be deposited from the vapor phase to reach high performance. Vapor deposition is preferred because it delivers ångström-level thickness control and virtually defect-free interfaces. However, the capital cost, limited throughput, and poor scalability of vacuum tools hinder large area manufacturing, especially in cost-sensitive markets such as consumer electronics and automotive sensing, wearables, IoT nodes, and low-cost machine vision. Solution processing is compatible with low-cost production, but in multi-layer stacks each new wet layer is cast in the presence of solvents that can redissolve or swell the underlying film and disturb crystal nucleation, so the probability of pinholes, interface roughening, and lattice disorder grows quasi-exponentially with every additional coat.[12–14] To address these issues, we restricted solution processing to a single active layer and reduced vapor deposition to a single electrode. Our device adopts a lateral MSM architecture with interdigitated electrodes (Fig. 4a) combined with a single BHJ layer comprising the low-bandgap polymer **TIIG-Se-DFT** blended with the NFA Y6 (Fig. 4a and b).

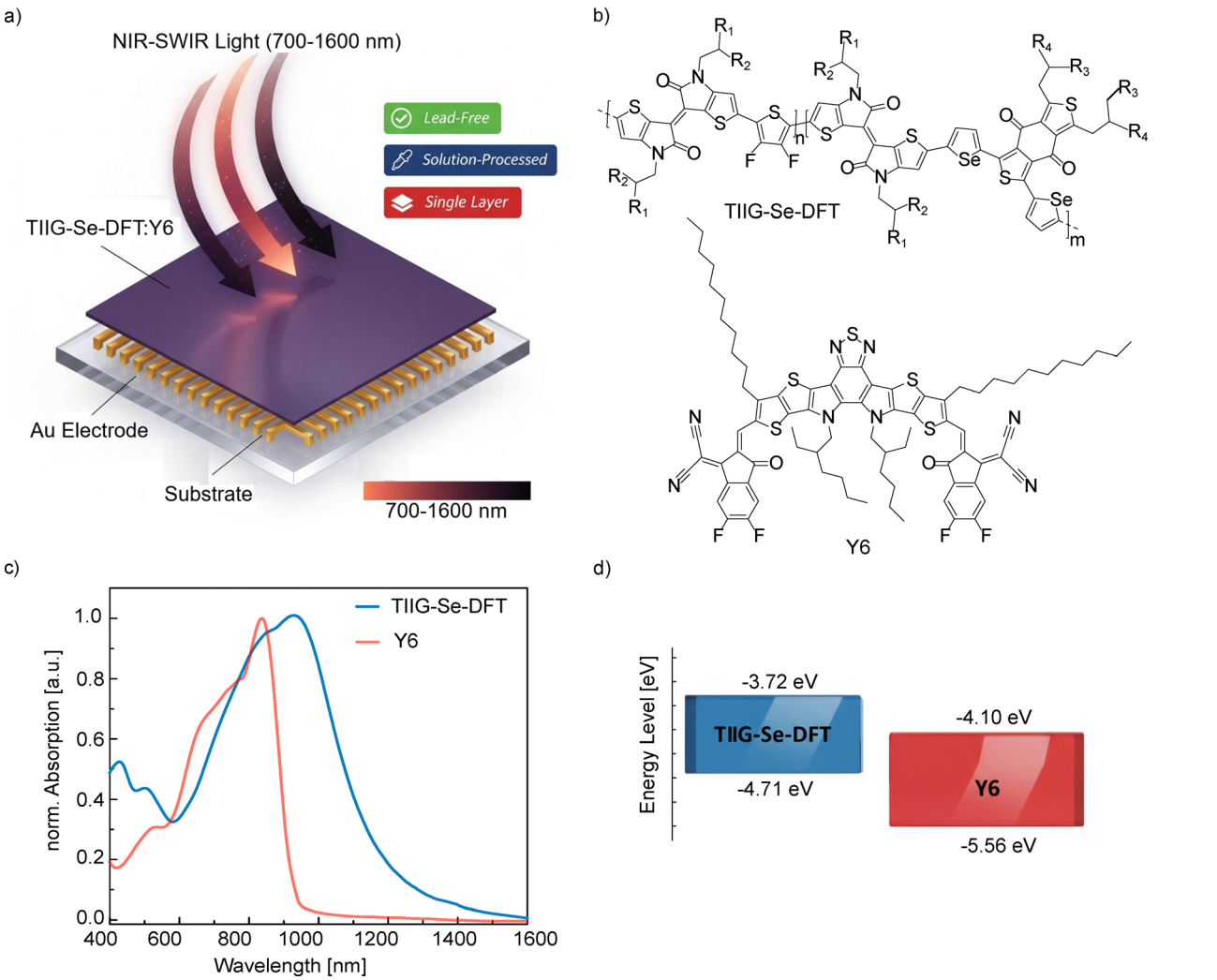

Fig. 4 Lead-free, solution-processed, single film NIR-SWIR OPD based on the **TIIG-Se-DFT**:Y6 blend: (a) Device schematic of the interdigitated MSM design for single layer thin film deposition enabling scalable production for consumer electronics, driver assistance, wearables, IoT nodes, and low-cost machine vision. (b) Chemical structures of the BHJ components: the **TIIG-Se-DFT** polymer ($R_1 = C_{10}H_{21}$, $R_2 = C_8H_{17}$, $R_3 = C_4H_9$, $R_4 = C_2H_7$) and the NFA Y6. (c) UV-vis-NIR absorption spectra of the donor (**TIIG-Se-DFT**, blue) and acceptor (Y6, red) highlighting their complementary, broadband absorption that extends deep into the SWIR. (d) Energy-level diagram for **TIIG-Se-DFT** and Y6, indicating efficient charge separation. The HOMO and LUMO levels of **TIIG-Se-DFT** were obtained from cyclic voltammetry measurements, whereas the Y6 energy levels were taken from literature.[46]

Open Access Article. Published on 03 June 2026. Downloaded on 6/4/2026 12:36:40 AM. This article is licensed under a Creative Commons Attribution 3.0 Unported Licence.

Optical characterization (Fig. 4c) demonstrates complementary absorption of the blend components: Y6 absorbs strongly in the 700–950 nm region with a peak at 840 nm, aligning well with previous reports.[45] **TIIG-Se-DFT** extends absorption into SWIR, showing a peak at 930 nm and a $\lambda_{cut\text{-}off}$ around 1600 nm. The films exhibit high absorption coefficients of 2.3×10^5 cm^{-1} for Y6 and 1.1×10^5 cm^{-1} for **TIIG-Se-DFT** (Fig. S2), enabling effective IR photon harvesting and enhanced detection sensitivity. The energy-level alignment between **TIIG-Se-DFT** and Y6[46] suggests a facilitated efficient exciton dissociation and charge transfer at the (D)–(A) interface (Fig. 4d). The **TIIG-Se-DFT** polymer's narrow optical bandgap ($\approx$ 0.96 eV) supports photodetection beyond the 1100 nm silicon limit, extending well into the SWIR region. FTIR spectroscopy confirms the presence and uniform distribution of the (D)–(A) components within the BHJ film (Fig. S5). Characteristic peaks for Y6 (C═O stretch at 1695 cm^{-1}, S–N stretch at 1535 cm^{-1}) and **TIIG-Se-DFT** (1635 cm^{-1}, 756 cm^{-1}) are distinctly observed, indicating successful incorporation and blending.

In summary, the key advantages of our approach are: a single active layer solution-processed under mild conditions ($\leq$100 °C, atmospheric pressure) combined with strong SWIR sensitivity, device simplicity, and environmental safety. Compared to conventional multilayer OPDs, our simplified method reduces fabrication complexity, cost, and reliance on vacuum deposition, while maintaining high SWIR performance. Moreover, avoiding toxic heavy metals such as Pb, Cd, or Hg ensures RoHS compliance and environmental safety, positioning our platform for diverse, high-volume applications. Table 2 reports competitive SWIR performance and scalability of our device *versus* TIIG-based state-of-the-art OPDs, enabled by minimal use of vacuum processes. Details of the device architectures are provided in Fig. S4. Employing NFAs like Y6 additionally provides broader absorption, improved morphological stability, and energy level tunability compared to fullerene acceptors such as PCBM, enhancing overall optoelectronic performance.[47]

To assess both the morphology and compositional uniformity of the active layer, NanoFTIR combined with AFM was performed on the **TIIG-Se-DFT**:Y6 blend films. Fig. S6 in the SI presents the topography (left) and optical phase (right) images of the **TIIG-Se-DFT**:Y6 film, revealing smooth and continuous surface morphology. Additionally, near-field NanoFTIR spectra acquired from two points (Fig. S6: region (I), dark green; region (II), bright green) showed nearly identical spectral features which confirms the formation of a spatially homogeneous BHJ. The lower panel highlights the far-field FTIR measurements for the single-component films: **TIIG-Se-DFT** (blue) and Y6 (red), revealing that both materials, **TIIG-Se-DFT** (1643 cm^{-1}) and Y6 (1681 cm^{-1}), are effectively integrated into the BHJ. The phase-uniform NanoFTIR response indicates a spatially homogeneous BHJ at the nanoscale for the optimized **TIIG-Se-DFT** : Y6 film (6 : 1 ratio). Complementary GIWAXS was performed on the device-relevant donor-rich **TIIG-Se-DFT** : Y6 blend (6 : 1) as well as on the neat components (Fig. S7a–c). The blend shows a distinct π–π stacking feature, evidencing short-range π–π ordering in the solid state.[48,49] Importantly, comparison with the neat films indicates that the donor-rich blend more closely resembles the neat **TIIG-Se-DFT** pattern (Fig. S7a and c), while the crystallinity and long-range ordering of neat Y6 is strongly attenuated under these donor-rich blending conditions (Fig. S7b and c). The π–π intensity is distributed over the full azimuthal range indicating slight face-on, but mostly isotropic orientation. Overall, these results support the presence of locally π-stacked domains in the final photoactive layer used in the champion devices and are consistent with our quantum-chemical calculations on the donor polymer. This suggests a tendency to form local π-stacked aggregates (Fig. 2). Variations in molecular weight are therefore expected to influence phase separation, domain formation, aggregation behavior, and film formation, thereby affecting charge-transport pathways and overall device performance. The mostly isotropic, well-intermixed blend morphology favors balanced carrier pathways which is critical for achieving both high detectivity and fast transient response. Collectively, the analyses of optical absorption, energetic alignment, chemical integration, and morphology emphasize that **TIIG-Se-DFT**:Y6 forms a promising, cost-effective BHJ system for high-performance organic NIR-SWIR photodetectors.

Fig. S8 illustrates the energy-band diagrams of the MSM photodetector under applied bias in the dark (Fig. S8a) and under illumination (Fig. S8b). In the MSM architecture, the two Au electrodes form back-to-back Schottky contacts[50] with the **TIIG-Se-DFT**:Y6 bulk heterojunction, such that the dark current is governed primarily by Schottky-barrier-limited carrier injection.[17,18] Under applied bias (Fig. S8a), one contact is effectively forward biased while the other is reverse biased. Under SWIR illumination (Fig. S8b), excitons generated in the donor–acceptor blend dissociate at the interface, and the resulting carriers are separated and transported laterally by this external field.

Table 2 The best TIIG-based NIR-SWIR OPDs benchmarked against device structure: vacuum- *vs.* solution deposited layers

TIIG-family	Spectral response [nm]	D^* 1200 nm [Jones]	D^* 1550 nm [Jones]	Solution depos. layers	Vapor depos. layers	Device type	Process-complexity level
TIIG-Se-DFT (this work)	400–1600	0.93×10^{11}	1.24×10^9	1	1	MSM (IDE)	🟩⬜⬜
TRA-TIIG-TRA[36]	300–900	No SWIR	No SWIR	2	3	Vert. stack	🟥🟥🟥
TIIG-T-OC[34]	300–900	No SWIR	No SWIR	3	2	Vert. stack	🟨🟨⬜
TIIQ[35]	NA	NA	NA	1	3	Vert. stack	🟥🟥🟥
PDT[33]	400–1600	6.03×10^{11}	6.00×10^{10}	2	3	Vert. stack	🟥🟥🟥

🟩 Single solution layer + 1 metal. 🟨 ≥2 vacuum step stacks. 🟥 ≥3 vacuum step stacks.

This journal is © The Royal Society of Chemistry 2026

Open Access Article. Published on 03 June 2026. Downloaded on 6/4/2026 12:36:40 AM.
This article is licensed under a Creative Commons Attribution 3.0 Unported Licence.

Consistent with this mechanism, the responsivity of the **TIIG-Se-DFT**:Y6 MSM-IDE devices rises with both increasing applied bias and decreasing inter-finger gap (Fig. S9), confirming that stronger lateral fields and shorter carrier transit paths improve carrier collection efficiency.[51,52] These results support field-assisted photoconductive MSM operation.

2.3. Photodetector characterization

Devices were fabricated with **TIIG-Se-DFT** : Y6 BHJs spanning (D)–(A) weight ratios of 2 : 1, 4 : 1, and 6 : 1 to pinpoint the optimum photodetector composition. As detailed in Fig. S10, raising the donor fraction progressively amplifies the SWIR tail while the Y6 network still furnishes continuous electron pathways. The 6 : 1 blend (Fig. 5) emerges as a clear "sweet spot": its specific detectivity at the eye-safe 1550 nm line is $\approx 3\times$ and $\approx 9\times$ higher than those of the 4 : 1 and 2 : 1 devices, respectively, and its spectrum shows markedly enhanced photocurrent, consistent with lower noise density. Concurrently, the Y6 Q-band shoulder at ≈900 nm red-shifts and diminishes, reflecting dilution of pure Y6 domains and stronger (D)–(A) electronic coupling. Attempts to increase the donor fraction further (8 : 1) led to aggregate-rich films with negligible photoconductivity, underscoring that 6 : 1 provides the optimal balance between SWIR photon harvesting and charge transport. Fig. 5a illustrates the dark current density–voltage (J–V) characteristics of the optimized device. The photodetector demonstrates near-symmetric response under positive and negative bias and low dark current densities of approximately 4.6×10^{-8} A cm^{-2} at 1 V_{bias} and 4.7×10^{-7} A cm^{-2} at 5 V_{bias}, respectively. This low dark current is crucial for high sensitivity. The responsivity (R) curve presented in Fig. 5b shows the device's efficiency in converting incident photons into electrical signals. The photodetector exhibits a wide spectral responsivity, extending broadly from 400 nm into the SWIR region, with a notable maximum responsivity (R_{max}) of approximately 0.05 A W^{-1} observed at around 1150 nm. The comparatively large active-layer thickness (≈920 nm, Fig. S11) is beneficial for SWIR detection, as it increases the optical path length and enhances absorption in the long-wavelength region. This is consistent with previous reports demonstrating that increasing the active-layer thickness is necessary to improve absorption and photocurrent generation in SWIR semiconductor devices.[53]

This performance significantly exceeds the detection capability of conventional silicon-based photodetectors, which typically show a steep drop-off beyond ≈1000 nm. Hence, the developed organic photodetector represents a promising candidate for SWIR detection applications, particularly where flexibility and cost-effectiveness are desired. In Fig. 5c, the specific detectivity (D^*) curves are presented under applied biases of 1 V, 2 V, and 5 V. Notably, the organic photodetector achieves D^* values higher than 1×10^{11} Jones in the critical wavelength range between 1050 nm and 1190 nm at 5 V_{bias}. This exceptional detectivity is primarily attributable to the device's low dark current, a consequence of the polymer's deep HOMO level (−4.71 eV) and its planar backbone geometry enabled by F···X (X = S, H) and Se interactions. These features minimize thermal excitation and suppress leakage pathways, enhancing the signal-to-noise ratio. At 1550 nm, the device maintains a responsivity of ≈0.02 A W^{-1}, comparable to one of the best TIIG-based SWIR detectors reported by Han *et al.*, which uses a complex vertical five-layer stacked structure. This sustained SWIR response, despite reduced photon energy, highlights efficient exciton dissociation and low recombination losses, a direct outcome of optimized (D)–(A) alignment and balanced charge mobility. These enhancements underscore the effectiveness of our molecular engineering and MSM architecture in overcoming the long-standing tradeoffs between spectral reach, signal strength, and fabrication simplicity in organic SWIR photodetectors.

2.4. Scientific background on photodetector metrics

To evaluate the optoelectronic performance of the polymer SWIR photodetector, several key figures of merit are considered, including on:off ratio, responsivity (R), specific detectivity

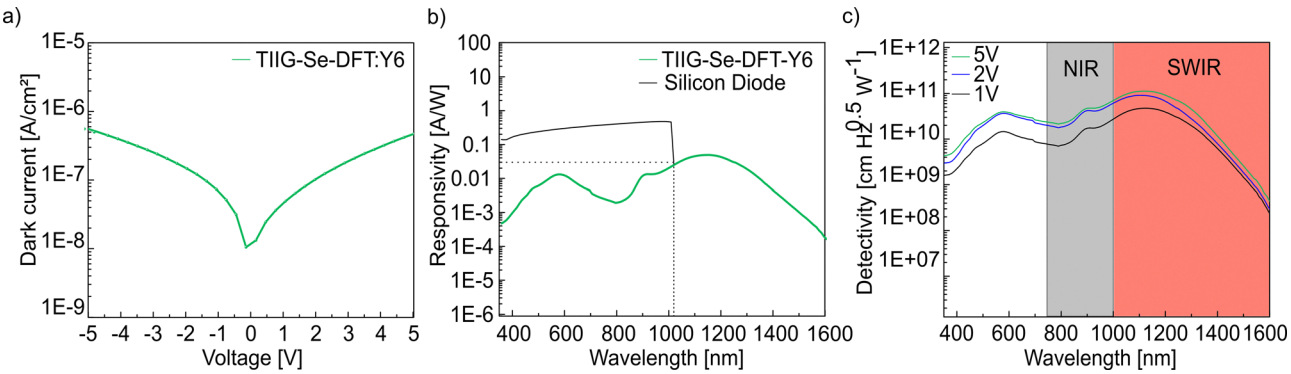

Fig. 5 Photodetector characterization of optimized BHJ (**TIIG-Se-DFT** : Y6, 6 : 1) organic photodetector. (a) Dark current–voltage (J–V) characteristics measured under bias voltages ranging from −5 V to +5 V, highlighting low leakage currents essential for high device sensitivity. (b) Spectral responsivity of the optimized organic photodetector (blue solid line), demonstrating a broad photoresponse extending from 400–1600 nm, with a maximum responsivity (R_{max} ≈ 0.05 A W^{-1}) around 1150 nm, surpassing the NIR detection limits of commercial silicon photodiodes (black line, K1713-08 Hamamatsu). (c) Specific detectivity spectra under varying bias conditions (1 V, 2 V, and 5 V), revealing significant D^* exceeding 1×10^{11} Jones in the critical NIR-SWIR region (1050–1190 nm) and maintaining values above 1.3×10^{9} Jones at technologically relevant wavelengths up to 1550 nm.

Open Access Article. Published on 03 June 2026. Downloaded on 6/4/2026 12:36:40 AM. This article is licensed under a Creative Commons Attribution 3.0 Unported Licence.

(D^*), noise current, and temporal response. These parameters provide a quantitative framework for benchmarking detector efficiency, spectral reach, and noise performance under practical illumination conditions.

on:off ratio: is defined as the ratio of the photocurrent I_{ph} generated under incident photon-radiation to the dark current I_{dark}, reflecting the amplification efficiency of photogenerated charge carriers[54] according to eqn (1):[54]

$$\text{on:off} = \frac{I_{ph}}{I_{dark}} \quad (1)$$

This figure of merit reflects the detector's ability to clearly distinguish between illuminated and dark states. A high on:off ratio is essential for improving the contrast and accuracy in switching and imaging applications.

Responsivity (R): quantifies the efficiency with which incident optical power is converted into electrical current.[55] The responsivity of a photodetector is the ratio of its output electrical signal, a current I_{out}, to the input optical signal expressed in terms of the incident optical power P_{in} according to eqn (2):[54]

$$R = \frac{I_{out}}{P_{in}};\ \text{with}\ P_{in} = \Phi_{ph} \times A \times \frac{hc}{\lambda} \quad (2)$$

where A is the detector area, Φ_{ph} is the photon flux density (photons m^{-2} s^{-1}), h is Planck's constant, c is the speed of light, and λ is the incident light wavelength. Responsivity is a wavelength-dependent parameter. High values in the SWIR, particularly at 1550 nm, are critical for applications in fiber-optic communication, LiDAR, and SWIR imaging.

Specific detectivity D^*: is used to compare photodetectors with very different physical and operational characteristics and is expressed in units of Jones [cm $Hz^{\frac{1}{2}}$ W^{-1}]. The area A = 1 cm^2 and the electrical bandwidth Δf is 1 Hz. The sensitivity of the detector can be defined as the minimum detectable optical input power that can be sensed with a signal to noise ratio of unity. This power is called the noise-equivalent-power P_{NEP} of the detector. The specific detectivity is given by eqn (3):[55]

$$D^* = \frac{R}{I_{noise}};\ \text{with}\ P_{NEP} = \frac{I_{noise}}{R} \quad (3)$$

Temporal response (rise/fall time): rise time refers to the time it takes for the photocurrent to increase from 10% to 90% of its maximum value upon exposure to a light pulse. Conversely, fall time is the duration required for the photocurrent to decrease from 90% to 10% after the light is removed.[54] These parameters are essential for characterizing the dynamic behavior and switching speed of photodetectors. Fast rise and fall times indicate efficient charge transport and minimal recombination losses, making them critical for real-time applications such as optical communication, LiDAR, pulse-resolved sensing, and biomedical signal monitoring. In this work, sub-100 μs rise and fall times demonstrate the photodetector's capability to operate effectively under high speed or pulsed illumination conditions.

2.5. Technological evaluation and application prospects

To comprehensively evaluate the application potential of the new **TIIG-Se-DFT**:Y6-based organic photodetector, detailed device characterizations were conducted to assess performance across critical NIR and SWIR application domains (Fig. 6). Particular attention was given to quantitative metrics such as specific detectivity, linear dynamic range, temporal response, and physiological signal fidelity, parameters that determine device viability in fields such as fiber optic communication, biomedical diagnostics, and eye-safe remote sensing (*e.g.*, LiDAR at 1550 nm). Specific detectivity measurements across critical technological wavelengths, 850, 900, 1000, 1100, 1200, 1300, 1400, 1500, and 1550 nm, demonstrate consistently high performance throughout the targeted NIR-SWIR spectral range (Fig. 6a). Notably, the device achieved D^* values above 1.3 × 10^9 Jones at 1550 nm, a wavelength where organic detectors typically underperform due to intrinsic absorption limits and carrier mobility loss. This highlights the system's robustness in eye-safe, long-range optical communication. Reaching sustained D^* beyond 1400 nm underscores the efficacy of **TIIG-Se-DFT**:Y6 in extending photoresponse into the SWIR window relevant for atmospheric transparency and telecommunication applications. Photocurrent linearity with increasing optical intensity (Fig. 6b) confirms a broad dynamic range with minimal trap filling, highlighting efficient exciton dissociation and stable charge transport. This response supports accurate optical signal quantification under varying illumination, vital for biomedical diagnostics and photometric sensing. The approximately linear photocurrent–voltage relationship (Fig. 6c) reflects efficient field-assisted charge extraction under applied bias. This supports the material's use in tunable detection schemes where signal gain or operating regime must be dynamically adjusted, as in adaptive biomedical sensors or optical feedback circuits. Fig. 6d exhibits a bias-enhanced photoconductive I–V response, consistent with field-assisted charge extraction and Schottky-limited contact injection at the Au/BHJ interfaces.[50] In the lateral MSM layout, the two contacts effectively form back-to-back Schottky junctions. Under bias, one contact is forward biased while the other is reverse biased, so the reverse-biased barrier predominantly limits leakage and thereby reduces the dark current. This behavior yields a high on:off ratio (≈150; Fig. 6d), robust signal detection under low-flux conditions relevant to wearable diagnostics, night-time imaging, and precision sensing. The interdigitated geometry also produces a measurable zero-bias photocurrent, indicating efficient carrier separation by built-in interfacial fields, which supports low-power operation (*e.g.* at ≤1 V). Lastly, the near-symmetric response under positive and negative bias implies comparable interfacial barriers at both electrodes, enabling polarity-independent operation (forward or reverse bias) without degrading the measured output.[50]

Transient response measurements at 1200 nm (modulated at 200 Hz, 1 V_{bias}) revealed fast rise (≈86 μs) and fall (≈36 μs) times (Fig. 6e), confirming efficient charge generation and extraction, likely aided by strong (D)–(A) coupling and suppressed recombination. These sub-100 μs dynamics validate the

This journal is © The Royal Society of Chemistry 2026

Open Access Article. Published on 03 June 2026. Downloaded on 6/4/2026 12:36:40 AM.
This article is licensed under a Creative Commons Attribution 3.0 Unported Licence.

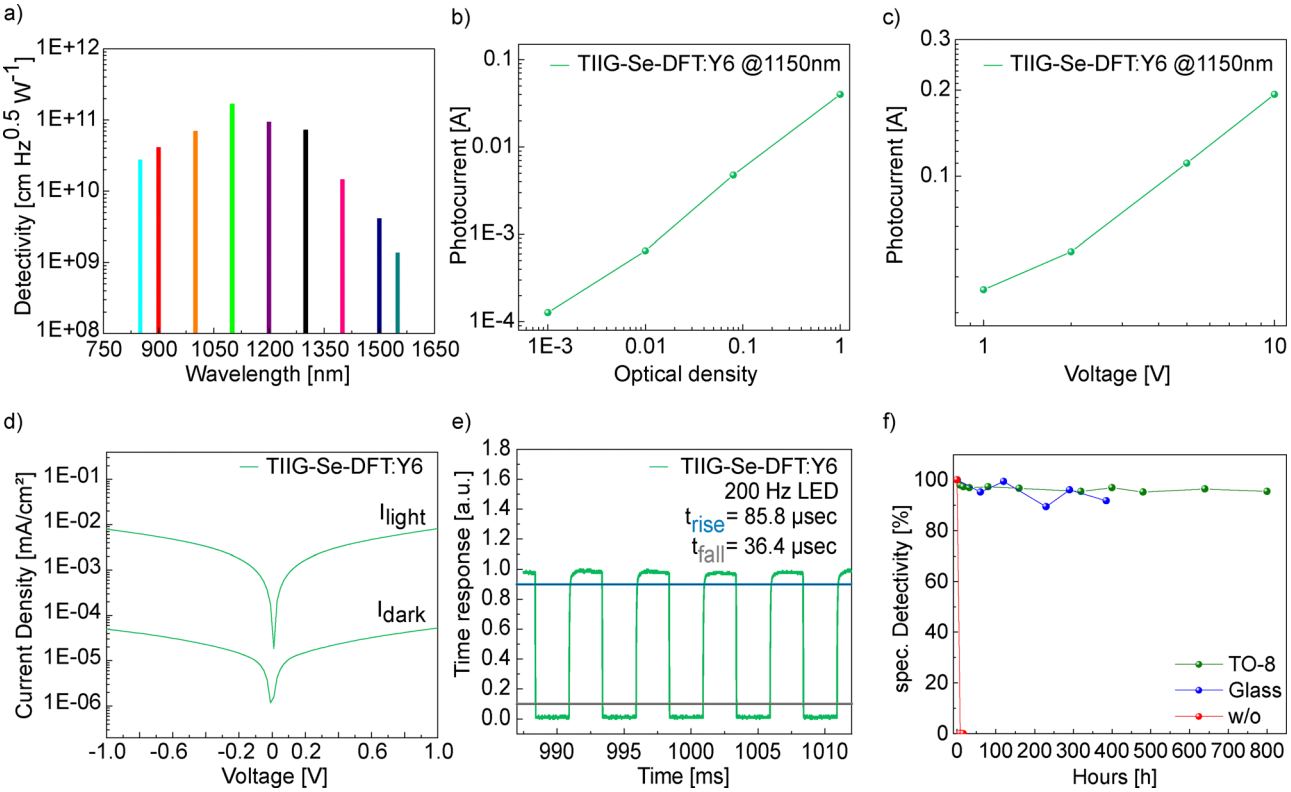

Fig. 6 Comprehensive characterization and application-oriented evaluation of **TIIG-Se-DFT**:Y6-based organic photodetectors: (a) Specific detectivity measured at key wavelengths across the NIR-range: 850 nm (2.8×10^{10} Jones), 900 nm (4.1×10^{10} Jones), 1000 nm (6.9×10^{10} Jones), 1100 nm (1.7×10^{11} Jones), 1200 nm (9.4×10^{10} Jones), 1300 nm (7.2×10^{10} Jones), 1400 nm (1.3×10^{10} Jones), 1500 nm (4.3×10^{9} Jones), and 1550 nm (1.4×10^{9} Jones), demonstrating consistently high detectivity values. (b) Photocurrent linearity as a function of optical intensity at 1150 nm (1 V_{bias}), indicating efficient photon to electron conversion. (c) Photocurrent *versus* applied bias voltage at 1150 nm illumination, highlighting strong linear response and effective charge transport. (d) (*J*–*V*) characteristics comparing dark and illuminated conditions, illustrating a high photo to dark current ratio ($\approx 1.5 \times 10^{2}$), essential for sensitive and low-noise detection. (e) Temporal response analysis under pulsed illumination at 1200 nm (200 Hz, 1 V_{bias}), revealing fast rise ($\approx$86 µs) and fall ($\approx$36 µs) times. (f) Long-term stability tests of devices under three conditions: TO-8 metal-can encapsulation *vs.* glass-cover vs no encapsulation. TO-8 packaging (Fig. 6f, green) yields the highest stability, supporting its suitability for industrial applications. A batch, sealed with Kapton foil, UV-curable epoxy, and a glass cover, also maintained stable performance during 400 hours of testing in air at 80 °C as shown by the champion device (Fig. 6f, blue).

device's capability for real-time biomedical imaging and wearable pulse sensing. In contrast to traditional InGaAs or PbSe photodetectors, which require high temperature and vacuum processing, our single layer polymeric system achieves comparable SWIR detectivity using low-cost, RoHS-compliant materials, marking a decisive step toward sustainable photonics. Lastly, to evaluate long-term viability, packaging stability tests were performed: TO-8 metal can encapsulation (Fig. 6f, green) preserved over 95% responsivity after 800 hours in dark ambient conditions, confirming environmental robustness and packaging compatibility for SWIR deployment. In contrast, unencapsulated devices (Fig. 6f, red) failed within several hours due to moisture and oxygen access. These results highlight the importance of robust encapsulation strategies, confirming TO-8 metal can packaging as a reliable solution for achieving industrial-grade stability in organic devices. Additional stability measurements on an independently fabricated batch, encapsulated with Kapton foil, UV-curable epoxy, and a glass cover, showed good stability over a 400 hours test period in air at 80 °C (Fig. 6f).

In summary, the **TIIG-Se-DFT**:Y6 system sets high performance standards for organic photodetectors, demonstrating broadband NIR-to-SWIR detection up to 1600 nm, sub-100 µs response times, low dark currents, and high operational stability. Its simplified single film MSM device architecture ensures solution-processability, RoHS compliance, and scalability, making it highly suitable for wearable diagnostics, SWIR-LiDAR, and cost-sensitive photonic applications.

3. Conclusion

In this study, we designed, synthesized, and characterized a novel ultralow bandgap thienoisoindigo-based conjugated polymer, **TIIG-Se-DFT**, tailored for broadband NIR-SWIR photodetection. Through the strategic incorporation of electron-rich selenophene units and fluorinated thiophene moieties, **TIIG-Se-DFT** achieves a low optical bandgap of 0.96 eV, high absorption coefficients, high thermal stability and an extended absorption edge beyond 1600 nm, surpassing the spectral limits of conventional silicon-based detectors.

Open Access Article. Published on 03 June 2026. Downloaded on 6/4/2026 12:36:40 AM. This article is licensed under a Creative Commons Attribution 3.0 Unported Licence.

When blended with the nonfullerene acceptor Y6 in a solution-processed BHJ and integrated into a simple metal-semiconductor–metal device architecture, the resulting photodetector exhibits a peak specific detectivity of $\approx 2 \times 10^{11}$ Jones at 1150 nm and maintains strong detectivity ($\approx 0.13 \times 10^{10}$ Jones) at 1550 nm, a wavelength critical for fiber-optic communication, LiDAR, and biomedical imaging. Application driven assessments revealed fast transient response (rise/fall times of ≈86/36 μs), linear photocurrent behavior, and a strong signal-to-noise ratio, demonstrating suitability for low-power, real-time sensing platforms.

The simplified device architecture features a single solution-processed active layer, effectively avoids challenges with sequential multilayer solvent processing, such as crystallization disturbances, defect formation, and solvent-induced interlayer damage. It also eliminates the need for complex multilayer vacuum deposition, offering a pathway toward cost-effective, scalable, and environmentally friendly fabrication, compatible with roll-to-roll manufacturing. Consequently, **TIIG-Se-DFT**:Y6 emerges as a resource-efficient, scalable, and robust photodetection platform ideally suited for flexible electronics, wearable diagnostics, and cost-effective NIR-SWIR detection technologies.

4. Experimental section

4.1. Materials

All commercially available solvents, reagents, and chemicals were used as received without further purification unless otherwise stated. 1,3-Bis(5-trimethylstannylselenophen-2-yl)-5,7-bis-(2-ethylhexyl)benzo[1,2-*c*:4,5-*c*′]dithiophene-4,8-dione (DTD-Se), 3,4-difluoro-2,5-bis(trimethylstannyl)thiophene (DFT) and (E)-2,2′-dibromo-4,4′-bis(2-octyldodecyl)-[6,6′-bithieno[3,2-*b*]pyrrolylidene]-5,5′(4*H*,4′*H*)-dione (TIIG) were purchased from Ossila and Solarmer. Unless otherwise stated, all reactions were carried out under argon using standard Schlenk line techniques.

4.2. TIIG-Se-DFT synthesis

In a microwave vial, 1 mmol of TIIG was mixed with DTD-Se and DFT in a molar ratio of 1 : 0.80 : 0.20. The solid powder mixture was dissolved in anhydrous chlorobenzene (0.5 mL) followed by addition of tetrakis(triphenylphosphine)palladium(0) (2 mol-%, 5.02 mg), the resultant mixture was degassed for 30 min with argon and securely sealed. The glass vial was placed into a microwave reactor and heated at 140 °C for 2 min, 160 °C for 2 min, and followed by 180 °C for 30 min. After being cooled to room temperature, the reaction mixture was precipitated into a mixture of methanol (200 mL) and concentrated HCl (2 mL) and stirred for 1 h at RT. The precipitate was filtered and extracted (Soxhlet) with methanol, acetone, *n*-hexane, chloroform. The remaining polymer was dissolved in chlorobenzene and precipitated into methanol, filtered and dried under vacuum to achieve the desired polymers as a dark green solid.

4.3. Preparation of BHJ blends

The blends were prepared by dissolving the donor polymer and the NFA acceptor separately in dichlorobenzene with final concentrations for **TIIG-Se-DFT** (20 mg mL^{-1}) and Y6 (20 mg mL^{-1}), in a nitrogen-filled glove box. The solutions were stirred for 12 h at 70 °C, and then the donor and acceptor inks were mixed (2 : 1, 4 : 1, 6 : 1, 8 : 1 vol vol^{-1}) and stirred (2.5 h) to form the final blend ink.

4.4. Device fabrication

Interdigitated gold electrodes were cleaned prior to casting by sequential ultrasonication: 10 min in distilled water, 10 min in acetone, and 10 min in isopropanol. Final blend inks were then cast onto the interdigitated electrodes. To remove residual solvent and densify the films, the devices were annealed at 100 °C for 10 min under an inert atmosphere. For TO-8 packaging, devices were mounted on TO-8 sockets and encapsulated with caps equipped with an IR-transparent sapphire window under argon.

4.5. UV-vis-absorption spectroscopy

The absorption was measured in a QS quartz glass cuvette and on coated glass substrates with the PerkinElmer Lambda 1050 UV/vis/IR absorption photometer with an integrating sphere equipped with a Si-PMT and an InGaAs detector.

4.6. Computational

The optimized segments, repeating units, dimer and trimer alignments were obtained by initially modelling the molecules using Avogadro2 version 1.1. To reduce computational complexity, branched alkyl chains were replaced with methyl groups, as also reported in the literature.[9] The geometry of the units was pre-optimized using a universal force field (UFF) with conjugated gradient method. The units were again preoptimized by the extended tight binding semi-empirical xtb program package[40] using the ANCopt optimizer with 5×10^{-6} Eh energy convergence and 1×10^{-3} Eh α^{-1} gradient convergence. Afterwards an extensive conformer search was performed using the Conformer-Rotamer Ensemble Sampling Tool (CREST) at the GFN2-xTB level[56–58] in a 6 kcal mol^{-1} energy window at room temperature (298.15 K). The respective lowest conformers as well as selected higher order conformers were final geometry optimized by density functional theory at the ωB97X-D4/def2-SVP level[41] using ORCA 6.1.[59] followed by frequency calculations at the same level to ensure true minima. The resolution-of-identity (RI) approximation with the corresponding def2/J auxiliary basis set was employed together with the RIJCOSX approximation to accelerate the evaluation of Coulomb and exchange integrals. Single-point energies were performed on the ωB97X-D4/def2-TZVP level. To support the noncovalent dimer interactions, the ωB97X-D4 functional includes D4 dispersion correction. All structures were fully optimized using tight convergence criteria for both the self-consistent field (SCF) procedure and geometry optimization TightSCF and TightOpt settings. For the stacking experiments the units were placed perpendicular against each other according to three different repeating unit combinations (TIIG-DFT and TIIG-DFT, TIIG-DTD-Se and TIIG-DTD-Se as well as TIIG-DFT and TIIG-DTD-Se), as shown in Fig. S13, and again optimized starting with the CREST conformer search. Molecular

 This journal is © The Royal Society of Chemistry 2026

Open Access Article. Published on 03 June 2026. Downloaded on 6/4/2026 12:36:40 AM. This article is licensed under a Creative Commons Attribution 3.0 Unported Licence.

structures and electrostatic potential surfaces were visualized using UCSF ChimeraX (version 1.11.1).[60]

4.7. Gel permeation chromatography (GPC)

Number-average (M_n) was determined by Agilent Technologies 1200 series GPC running in chlorobenzene at 80 °C, using two PL mixed B columns in series, and calibrated against narrow polydispersity polystyrene standards.

4.8. Fourier-transform infrared spectroscopy (FTIR)

Measurements were performed with a Bruker Vertex 70 FTIR instrument by focusing the light of a globar as a MIR light source through a KBr beam splitter with integrated gold mirrors and an ATR sample stage with a Ge crystal. The spectra were recorded with an N_2 cooled MCT detector at a resolution of 2 cm^{-1} and averaged over 128 scans.

4.9. Atomic force microscopy (AFM) and nanoFTIR

The AFM and near field optical measurements were carried out using a commercial NeaSNOM system (Attocube Systems AG). The AFM was operated in tapping mode with Arrow-NCPT probes (Nanoworld). The free tapping amplitude of 80 nm was used. A broadband mid-IR laser source from Toptica Photonics AG is coupled to the asymmetric Michelson interferometer of the NeaSNOM and detected with a mercury cadmium telluride detector.

4.10. Grazing-incidence wide-angle X-ray scattering (GIWAXS)

Measurements were carried out on an Anton-Paar SAXSpoint 2.0 with a Primux 100 microfocus source using Cu-Kα_1 radiation (λ = 1.5406 Å) and a Dectris Eiger R 1 M 2D detector. The incident angle was 0.4° and the sample-detector distance was 140 mm.

4.11. Thermogravimetric analysis (TGA) and differential scanning calorimeter (DSC)

Measurements were performed using a Netzsch Jupiter ST 449 C instrument equipped with a Netzsch TASC 414/4 controller. The samples were heated from room temperature to 900 °C under nitrogen flow (25 mL min^{-1}) at a heating rate of 10 K min^{-1}.

4.12. Cyclic voltammetry (CV)

Measurements of polymer films were performed under argon atmosphere using a CHI760E Voltammetry analyzer with 0.1 M tetra-n-butylammonium hexafluorophosphate in acetonitrile as the supporting electrolyte. A platinum disk working electrode, a platinum wire counter electrode, and a silver wire reference electrode were employed, and the ferrocene/ferrocenium (Fc/Fc^+) was used as the internal reference for all measurements. The scanning rate was 100 mV s^{-1}. Polymer films were cast from chloroform solutions on a Pt working electrode (2 mm in diameter).

4.13. *J–V* curves

Were recorded with a Keithley 2401 source meter and a 170 W halogen lamp on a Bentham Instruments power supply.

4.14. Responsivity and detectivity

Were recorded with a home-built setup, consisting of a 170 W halogen lamp on a Bentham Instruments power supply. The light was chopped at a frequency of 100 Hz and a Quantum Design MSH 300 monochromator was used. The signal was amplified by a Stanford Research Systems SR830 Lock-In amplifier. The home-built setup is calibrated with an InGaAs photodiode from Hamamatsu (800–1800 nm). A Keithley 2401 source meter was used to apply bias voltage. A set of optical bandpass filters from Hamamatsu (850–1550 nm) was used to carry out the filter experiments. For light-intensity dependency measurements the home-built setup was equipped with a set of optical density filters (Thorlabs).

4.15. Response time

Rise and fall times of the detector were measured using a 1200 nm LED (Thorlabs, LED1200L) at a modulation frequency of 200 Hz. A waveform generator (Keysight 33500B) and an LED-Controller LDC202C (Thorlabs) were used to modulate the light frequency. An oscilloscope (Keysight InfiniiVision DSOX2024A) was used to measure the response time.

Author contributions

Rico Holfeuer (conceptualization: equal; data curation: lead; investigation: lead; project administration: lead; software: equal; validation: lead; visualization: lead; writing – original draft: lead; writing – review & editing: lead). Marc Comi (investigation: supporting; validation: supporting; visualization: supporting; writing – review & editing: supporting). Stefan Schröder (data curation: supporting; investigation: supporting; software: equal; visualization: supporting; writing – review & editing: supporting). Johannes Hofmann (data curation: supporting; visualization: supporting). Meriem Bouraoui (data curation: supporting; investigation: supporting; visualization: supporting). Johannes Hofmann (data curation: supporting; visualization: supporting). Rik Hooijer (data curation: supporting; investigation: supporting; visualization: supporting). Erkan Aydin (data curation: supporting; investigation: supporting; resources: supporting). Achim Hartschuh (data curation: supporting; funding acquisition: supporting; investigation: supporting; methodology: supporting; resources: supporting; validation: supporting). Mohammed Al-Hashimi (conceptualization: supporting; data curation: supporting; investigation: supporting; methodology: supporting; resources: supporting; visualization: supporting; writing – review & editing: supporting). AmirAbbas YousefiAmin (conceptualization: lead; data curation: supporting; funding acquisition: lead; investigation: supporting; project administration: supporting; resources: lead; supervision: lead; validation: supporting; visualization: supporting; writing – original draft: supporting; writing – review & editing: supporting). Tayebeh Ameri (conceptualization: equal; funding acquisition: supporting; investigation: supporting; project administration: supporting; resources: supporting; software: supporting; supervision: supporting; validation: supporting; writing – review & editing: supporting)

Open Access Article. Published on 03 June 2026. Downloaded on 6/4/2026 12:36:40 AM. This article is licensed under a Creative Commons Attribution 3.0 Unported Licence.

Conflicts of interest

The authors declare that they have no known competing financial interests or personal relationships that could have appeared to influence the work reported in this paper.

Data availability

The data that support the findings of this study are available in the supplementary information (SI) of this article. Supplementary information is available. See DOI: https://doi.org/10.1039/d5mh02371h.

Acknowledgements

The authors acknowledge funding from the DFG Excellence Cluster e-conversion (EXC 2089/1-390776260). T. A. acknowledges financial support of the DFG *via* the Heisenberg Program, project AM 519/4-1, and the collaborative research center CRC 1261, project number 286471992.

References

1 A. L. Antaris, H. Chen, S. Diao, Z. Ma, Z. Zhang and S. Zhu, *et al.*, A small-molecule dye for NIR-II imaging, *Nat. Mater.*, 2016, **15**(2), 235–242.
2 Q. Wu, D. Xu, X. Ma, Z. Li, Y. Qu and Z. Qiao, *et al.*, Study on 1550 nm Human Eye-Safe High-Power Tunnel Junction Quantum Well Laser, *Micromachines*, 2024, **15**(8), 1042.
3 R. Gao, F. Li, H. Yang, F. Yang, L. Lin and J. He, *et al.*, Highly flexible TFT monolithic-integrated (Bi,Sb)(2)Se(3) SWIR photodetector for wearable health monitoring and curved-surface imaging, *iScience*, 2025, **28**(3), 112008.
4 S. H. Kim, J. Lim, S. Lee, M. H. Kang, W. Song and J. Lim, *et al.*, Flexible hybrid photodetector based on silver sulfide nanoparticles and multi-walled carbon nanotubes, *RSC Adv.*, 2021, **11**(37), 22625–22632.
5 J. V. Dcosta, D. Ochoa and S. Sanaur, Recent Progress in Flexible and Wearable All Organic Photoplethysmography Sensors for SpO(2) Monitoring, *Adv. Sci.*, 2023, **10**(31), e2302752.
6 H. Anabestani, S. Nabavi and S. Bhadra, Advances in Flexible Organic Photodetectors: Materials and Applications, *Nanomaterials*, 2022, **12**(21), 3775.
7 C.-J. Lim, J.-H. Kim and J.-W. Park, Highly flexible and solution-processed organic photodiodes and their application to optical luminescent oxygen sensors, *Org. Electron.*, 2019, **65**, 100–109.
8 Z. Wang, S. Cheng, K. Fukuda, W. Hu, X. Xu and T. Someya, Flexible near-infrared organic photodetectors for emergent wearable applications, *Wearable Electron.*, 2024, **1**, 53–77.
9 B. Yin, X. Zhou, Y. Li, G. Hu, W. Wei and M. Yang, *et al.*, Sensitive Organic Photodetectors With Spectral Response up to 1.3 microm Using a Quinoidal Molecular Semiconductor, *Adv. Mater.*, 2024, **36**(19), e2310811.
10 X. Chen, Y. Zhu, Y. Xu, M. Rao, P. Pang and B. Zhang, *et al.*, Design of Ultra-Narrow Bandgap Polymer Acceptors for High-Sensitivity Flexible All-Polymer Short-Wavelength Infrared Photodetectors, *Angew. Chem., Int. Ed.*, 2025, **64**(2), e202413965.
11 Y. Wang, J. Wang, J. Miao, J. Liu and L. Wang, Using BODIPY Unit to Design Molecular Acceptors with Absorption Wavelength of >1000 nm for Organic Photodetectors, *CCS Chem.*, 2024, **6**(11), 2794–2803.
12 Z. Hu, F. Huang and Y. Cao, Layer-by-Layer Assembly of Multilayer Thin Films for Organic Optoelectronic Devices, *Small Methods*, 2017, **1**, 12.
13 L. Sun, K. Uemura, T. Takahashi, T. Yoshida and Y. Suzuri, Interfacial Engineering in Solution Processing of Silicon-Based Hybrid Multilayer for High Performance Thin Film Encapsulation, *ACS Appl. Mater. Interfaces*, 2019, **11**(46), 43425–43432.
14 H. Quan, Z. Zhong, T. Hao, K. An, W. Zhong and C. Wang, *et al.*, High-performance organic photodetectors enabled by a refined fibrillar multiphase morphology, *Chem. Eng. J.*, 2023, 452.
15 S. Habboush, S. Rojas, N. Rodríguez and A. Rivadeneyra, The Role of Interdigitated Electrodes in Printed and Flexible Electronics, *Sensors*, 2024, **24**, 9.
16 F. P. García de Arquer, A. Armin, P. Meredith and E. H. Sargent, Solution-processed semiconductors for next-generation photodetectors, *Nat. Rev. Mater.*, 2017, **2**, 3.
17 S. M. Sze, D. J. Coleman and A. Loya, Current transport in metal-semiconductor-metal (MSM) structures, *Solid-State Electron.*, 1971, **14**(12), 1209–1218.
18 J. B. D. Soole and H. Schumacher, InGaAs metal-semiconductor-metal photodetectors for long wavelength optical communications, *IEEE J. Quantum Electron.*, 1991, **27**(3), 737–752.
19 R. T. Tung, The physics and chemistry of the Schottky barrier height, *Appl. Phys. Rev.*, 2014, **1**, 1.
20 L. Tao, Z. Chen, X. Li, K. Yan and J.-B. Xu, Hybrid graphene tunneling photoconductor with interface engineering towards fast photoresponse and high responsivity, *npj 2D Mater. Appl.*, 2017, **1**, 1.
21 J. L. Li, J. J. Cao, L. L. Duan and H. L. Zhang, Evolution of Isoindigo-Based Electron-Deficient Units for Organic Electronics: From Natural Dyes to Organic Semiconductors, *Asian J. Org. Chem.*, 2018, **7**(11), 2147–2160.
22 T. Hasegawa, M. Ashizawa and H. Matsumoto, Design and structure–property relationship of benzothienoisoindigo in organic field effect transistors, *RSC Adv.*, 2015, **5**(75), 61035–61043.
23 D. Yoo, T. Hasegawa, M. Ashizawa, T. Kawamoto, H. Masunaga and T. Hikima, *et al.*, N-Unsubstituted thienoisoindigos: preparation, molecular packing and ambipolar organic field-effect transistors, *J. Mater. Chem. C*, 2017, **5**(10), 2509–2512.
24 O. Vybornyi, Y. Jiang, F. Baert, D. Demeter, J. Roncali and P. Blanchard, *et al.*, Solution-processable thienoisoindigo-based molecular donors for organic solar cells with high open-circuit voltage, *Dyes Pigm.*, 2015, **115**, 17–22.

 This journal is © The Royal Society of Chemistry 2026

Open Access Article. Published on 03 June 2026. Downloaded on 6/4/2026 12:36:40 AM. This article is licensed under a Creative Commons Attribution 3.0 Unported Licence.

25 C. Li, H. I. Un, J. Peng, M. Cai, X. Wang and J. Wang, *et al.*, Thiazoloisoindigo: A Building Block that Merges the Merits of Thienoisoindigo and Diazaisoindigo for Conjugated Polymers, *Chemistry*, 2018, **24**(39), 9807–9811.
26 Y. H. Wijsboom, Y. Sheynin, A. Patra, N. Zamoshchik, R. Vardimon and G. Leitus, *et al.*, Tuning of electronic properties and rigidity in PEDOT analogs, *J. Mater. Chem.*, 2011, **21**(5), 1368–1372.
27 H.-Y. Chen, S.-C. Yeh, C.-T. Chen and C.-T. Chen, Comparison of thiophene- and selenophene-bridged donor–acceptor low band-gap copolymers used in bulk-heterojunction organic photovoltaics, *J. Mater. Chem.*, 2012, **22**, 40.
28 A. Patra, R. Kumar and S. Chand, Selenium-Containing π-Conjugated Polymers for Organic Solar Cells, *Isr. J. Chem.*, 2014, **54**(5–6), 621–641.
29 Q. Fan, H. Fu, Q. Wu, Z. Wu, F. Lin and Z. Zhu, *et al.*, Multi-Selenophene-Containing Narrow Bandgap Polymer Acceptors for All-Polymer Solar Cells with over 15% Efficiency and High Reproducibility, *Angew. Chem., Int. Ed.*, 2021, **60**(29), 15935–15943.
30 S. Gámez-Valenzuela, M. Comí, S. R. González, M. C. R. Delgado, M. Al-Hashimi and R. Ponce Ortiz, The fluorination effect: the importance of backbone planarity in achieving high performance ambipolar field effect transistors, *J. Mater. Chem. C*, 2023, **11**(24), 8027–8036.
31 Z. Fei, P. Boufflet, S. Wood, J. Wade, J. Moriarty and E. Gann, *et al.*, Influence of Backbone Fluorination in Regioregular Poly(3-alkyl-4-fluoro)thiophenes, *J. Am. Chem. Soc.*, 2015, **137**(21), 6866–6879.
32 Y. Jiang, Y. Zhang, Y. Deng, S. Dong, B. Li and Y. Yi, *et al.*, Fusing Thienoisoindigo to the Conjugated Ribbons with Strong Absorption in the Second Near-Infrared Window, *CCS Chem.*, 2022, **4**(11), 3497–3504.
33 J. Han, J. Qi, X. Zheng, Y. Wang, L. Hu and C. Guo, *et al.*, Low-bandgap donor–acceptor polymers for photodetectors with photoresponsivity from 300 nm to 1600 nm, *J. Mater. Chem. C*, 2017, **5**(1), 159–165.
34 S. Guan and P. Guo, Synthesis of thiophene-isoindigo receptor small molecules and its application in photodetectors, *J. Phys.: Conf. Ser.*, 2024, **2730**, 1.
35 C. C. Lin, A. Velusamy, S. H. Tung, I. Osaka, M. C. Chen and C. L. Liu, Tunable Photoelectric Properties of n-Type Semiconducting Polymer:Small Molecule Blends for Red Light Sensing Phototransistors, *Adv. Opt. Mater.*, 2022, **10**, 10.
36 B.-H. Jiang, Y.-T. Liao, Y.-H. Tu, K.-T. Wong and C.-P. Chen, Solution-processed all-small-molecule organic photovoltaics and photodetectors based on isoindigo derivatives, *Dyes Pigm.*, 2023, 215.
37 Y. Chen, Y. Zheng, J. Wang, X. Zhao, G. Liu and Y. Lin, *et al.*, Ultranarrow-bandgap small-molecule acceptor enables sensitive SWIR detection and dynamic upconversion imaging, *Sci. Adv.*, 2024, **10**(23), eadm9631.
38 H. M. Luong, C. Kaiyasuan, A. Yi, S. Chae, B. M. Kim and P. Panoy, *et al.*, Highly Sensitive Resonance-Enhanced Organic Photodetectors for Shortwave Infrared Sensing, *ACS Energy Lett.*, 2024, **9**(4), 1446–1454.
39 G. Kim, H. Kim, M. Jang, Y. K. Jung, J. H. Oh and C. Yang, Ultra-narrow-bandgap thienoisoindigo polymers: structure–property correlations in field-effect transistors, *J. Mater. Chem. C*, 2016, **4**(40), 9554–9560.
40 C. Bannwarth, E. Caldeweyher, S. Ehlert, A. Hansen, P. Pracht and J. Seibert, *et al.*, Extended tight-binding quantum chemistry methods, *Wiley Interdiscip. Rev.: Comput. Mol. Sci.*, 2020, **11**, 2.
41 J. D. Chai and M. Head-Gordon, Systematic optimization of long-range corrected hybrid density functionals, *J. Chem. Phys.*, 2008, **128**(8), 084106.
42 Y. Bai, Z. Zhang, Q. Zhou, H. Geng, Q. Chen and S. Kim, *et al.*, Geometry design of tethered small-molecule acceptor enables highly stable and efficient polymer solar cells, *Nat. Commun.*, 2023, **14**(1), 2926.
43 Y. Zhang, L. Kong, Y. Zhang, H. Du, J. Zhao and S. Chen, *et al.*, Ultra-low-band gap thienoisoindigo-based ambipolar type neutral green copolymers with ProDOT and thiophene units as NIR electrochromic materials, *Org. Electron.*, 2020, **81**, 105685.
44 X. Liu, L. Kong, H. Du, Y. Zhang, J. Zhao and Y. Xie, Synthesis and electrochromic properties of electrochromic polymers based on propylenedioxythiophene, diketopyrrolopyrrole and benzodithiophene units, *Org. Electron.*, 2019, **64**, 223–235.
45 S. Y. Park, C. Labanti, R. A. Pacalaj, T. H. Lee, Y. Dong and Y. C. Chin, *et al.*, The State-of-the-Art Solution-Processed Single Component Organic Photodetectors Achieved by Strong Quenching of Intermolecular Emissive State and High Quadrupole Moment in Non-Fullerene Acceptors, *Adv. Mater.*, 2023, **35**(49), e2306655.
46 J. Yuan, Y. Zhang, L. Zhou, G. Zhang, H.-L. Yip and T.-K. Lau, *et al.*, Single-Junction Organic Solar Cell with over 15% Efficiency Using Fused-Ring Acceptor with Electron-Deficient Core, *Joule*, 2019, **3**(4), 1140–1151.
47 C. Yan, S. Barlow, Z. Wang, H. Yan, A. K. Y. Jen and S. R. Marder, *et al.*, Non-fullerene acceptors for organic solar cells, *Nat. Rev. Mater.*, 2018, **3**, 3.
48 Z. Peng, L. Ye and H. Ade, Understanding, quantifying, and controlling the molecular ordering of semiconducting polymers: from novices to experts and amorphous to perfect crystals, *Mater. Horiz.*, 2022, **9**(2), 577–606.
49 X. Xia, L. Mei, C. He, Z. Chen, N. Yao and M. Qin, *et al.*, Revealing the crystalline packing structure of Y6 in the active layer of organic solar cells: the critical role of solvent additives, *J. Mater. Chem. A*, 2023, **11**(40), 21895–21907.
50 M. Hasani, S. Hamedi and H. Dehdashti Jahromi, Experimental and theoretical analysis of a Visible-Light photodetector based on cadmium sulfide fabricated on interdigitated electrodes, *Results Phys.*, 2024, **56**, 107291.
51 N. Al-Khalli and N. Debbar, Performance enhancement of ZnO-based MSM photodiodes by optimizing structure parameters. International Journal of Numerical Modelling: Electronic Networks, *Devices Fields*, 2018, **32**, 2.

Open Access Article. Published on 03 June 2026. Downloaded on 6/4/2026 12:36:40 AM.
This article is licensed under a Creative Commons Attribution 3.0 Unported Licence.

52 N. Al-Khalli, M. Aboud and N. Debbar, Theoretical study and design of n-ZnO/p-Si heterojunction MSM photodiode for optimized performance, *Opt. Laser Technol.*, 2021, 133.
53 J. Z. Fan, M. Vafaie, K. Bertens, M. Sytnyk, J. M. Pina and L. K. Sagar, *et al.*, Micron Thick Colloidal Quantum Dot Solids, *Nano Lett.*, 2020, **20**(7), 5284–5291.
54 M. D. Ward, W. Shi, N. Gasparini, J. Nelson, J. Wade and M. J. Fuchter, Best practices in the measurement of circularly polarised photodetectors, *J. Mater. Chem. C*, 2022, **10**(29), 10452–10463.
55 M. Razeghi, *Technology of Quantum Devices*, Springer, New York, 2010, p. 560.
56 P. Pracht, F. Bohle and S. Grimme, Automated exploration of the low-energy chemical space with fast quantum chemical methods, *Phys. Chem. Chem. Phys.*, 2020, **22**(14), 7169–7192.
57 S. Grimme, Exploration of Chemical Compound, Conformer, and Reaction Space with Meta-Dynamics Simulations Based on Tight-Binding Quantum Chemical Calculations, *J. Chem. Theory Comput.*, 2019, **15**(5), 2847–2862.
58 P. Pracht, S. Grimme, C. Bannwarth, F. Bohle, S. Ehlert and G. Feldmann, *et al.*, CREST-A program for the exploration of low-energy molecular chemical space, *J. Chem. Phys.*, 2024, **160**(11), 114110.
59 F. Neese, Software Update: The ORCA Program System—Version 6.0, *Wiley Interdiscip. Rev.: Comput. Mol. Sci.*, 2025, **15**, 2.
60 E. C. Meng, T. D. Goddard, E. F. Pettersen, G. S. Couch, Z. J. Pearson and J. H. Morris, *et al.*, UCSF ChimeraX: Tools for structure building and analysis, *Protein Sci.*, 2023, **32**(11), e4792.

 This journal is © The Royal Society of Chemistry 2026